Nuclear Science and Techniques (2026) 37:63
https://doi.org/10.1007/s41365-026-01885-7

Design and optimization of a compact high-energy electron source applied to on-site non-destructive testing for electrical equipment

Hai-Meng Wang[1] · Yi-Feng Zeng[1] · Hao Hu[1] · Jun-Yang Li[1] · Tong-Ning Hu[1]

Received: 1 November 2023 / Revised: 26 September 2024 / Accepted: 21 October 2024 / Published online: 29 January 2026

Abstract

X-rays are widely used in the non-destructive testing (NDT) of electrical equipment. Radio frequency (RF) electron linear accelerators can generate MeV high-energy X-rays with strong penetrating ability; however, the system generally has a large scale, which is not suitable for on-site testing. Compared with the S-band (S-linac) at the same stage of beam energy, the accelerator working in the X-band (X-linac) can compress the facility scale by over 2/3 in the longitudinal direction, which is convenient for the on-site NDT of electrical equipment. To address the beam quality and design complexity simultaneously, the non-dominated sorting genetic algorithm II (NSGA-II), which is a multi-objective genetic algorithm (MOGA), was developed to optimize the cavity chain design of the X-linac. Additionally, the designs of the focusing coils, electron gun, and RF couplers, which are other key components of the X-linac, were introduced in this context. In particular, the focusing coil distributions were optimized using a genetic algorithm. Furthermore, after designing such key components, PARMELA software was adopted to perform beam dynamics calculations with the optimized accelerating fields and magnetic fields. The results show that the beam performance was obtained with a capture ratio of more than 90%, an energy spread of less than 10%, and an average energy of approximately 3 MeV. The design and simulation results indicate that the proposed NSGA-II-based approach is feasible for X-linac accelerator design. Furthermore, it can be generalized as a universal technique for industrial electron linear accelerators provided that specific optimization objectives and constraints are set according to different application scenarios and requirements.

Keywords Non-destructive testing · X-band linac accelerator · Focusing coils · Electron gun · Radio frequency couplers

1 Introduction

The holistic functionality of a large electrical apparatus can be impacted by the presence of internal imperfections, potentially resulting in power disruption. Consequently, the identification of latent defects in electrical infrastructure is essential and is typically performed using non-destructive testing (NDT). Traditional NDT technologies, such as infrared thermal imaging [1–5], ultraviolet imaging [6], ultrasonic [7], and eddy current [8], are employed for this purpose. However, the efficacy of these traditional methods is significantly hindered by constraints inherent in the material constitution, structural complexities, and contextual nuances of the designated application site. This intrinsic limitation poses a formidable obstacle to the provision of dependable and accurate evaluation of internal defects in a large electrical apparatus.

X-ray-based NDT uses highly penetrating electromagnetic waves to directly observe the internal structure of electrical equipment. In 2012, X-ray digital photography (DR) was utilized by the Yunnan Electric Power Research Institute to visually detect typical defects in gas-insulated switchgear (GIS). An X-ray DR system was demonstrated as feasible, safe, and effective for NDT [9]. Similar research was

---

Hai-Meng Wang, Yi-Feng Zeng, Hao Hu have contributed equally to this work.

This work was supported by the National Natural Science Foundation of China (Nos. 12341501 and 12575164).

✉ Tong-Ning Hu
TongningHu@hust.edu.cn

[1] State Key Laboratory of Advanced Electromagnetic Technology, School of Electrical and Electronic Engineering, Huazhong University of Science and Technology, Wuhan 430074, China

conducted by the Hebei Electric Power Research Institute in 2018. Furthermore, internal defects within GIS can be accurately diagnosed, and visual detection of GIS can be achieved using X-ray DR [10]. However, X-rays are typically propelled by an electron beam with an energy level of several hundred kilo-electron volts (keV), and their penetration capability often fails to meet the demands imposed by large-scale electrical equipment [11]. Therefore, it is imperative to enhance the output energy of the driving electron source. A radio frequency (RF) linear accelerator can supply an electron beam with energies on the order of several mega-electron volts (MeV) [12–14]. However, the traditional S-band accelerator and its affiliated power system are inherently massive and unsuitable for on-site NDT. Conversely, a high acceleration gradient and operating frequency can be achieved by using an X-band accelerator with a compact structure [15, 16]. Hence, the X-band accelerator has emerged as a pragmatic solution for the on-site NDT of electrical equipment.

In recent years, numerous accelerator laboratories have developed X-band accelerators [17–19]. In 2016, an acceleration gradient significantly exceeding 130 MV/m was achieved by the Istituto Nazionale di Fisica Nucleare using X-band accelerating structures [20]. In 2017, a prototype X-band 24-unit compact linear collider traveling wave (TW) accelerator was successfully prepared by Tsinghua University [21]. By 2018, three X-band test facilities, namely Xbox1, Xbox2, and Xbox3, were established by the European Organization for Nuclear Research [22]. In 2021, a 6 MeV X-band accelerator was designed by the American company RadiaBeam [23]. In 2022, the acceleration gradient of an X-band linac was improved by Tsinghua University to increase the electron beam energy from 50 to 350 MeV [24].

To generate MeV high-energy X-rays and achieve on-site NDT of electrical equipment, the key components of the X-band linac were devised. These components include a TW accelerating structure, focusing coil, electron gun, and RF couplers [25]. A comprehensive layout is shown in Fig. 1.

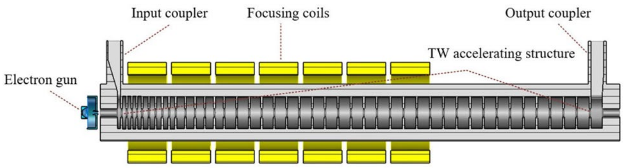

Fig. 1 (Color online) Accelerator layout

In the design of the phase velocity and longitudinal magnetic field of focusing coils, repeated attempts based on engineering experience are necessary, which is time-consuming and makes it difficult to achieve optimal performance. In 2002, a non-dominated sorting genetic algorithm II (NSGA-II) was proposed by Deb [26], which has good convergence and diversity in solving multi-objective problems and multi-constraint conditions. Many accelerator-related optimization problems have been solved by using intelligent algorithms [27–30]. Consequently, it is feasible to optimize the accelerator using a multi-objective genetic algorithm (MOGA) [31].

In this context, this study developed a universal MOGA for designing accelerator cavity chains under multiple constraints. Considering that the designed X-band linac can be applied to on-site NDT for electrical equipment, a linac cavity chain with low-energy spread, high output energy, and high capture rate was designed. Simultaneously, a low-energy spread accelerator was designed to validate the applicability of the proposed NSGA-II-based approach.

2 Fundamentals of a traveling wave accelerator

To design a TW accelerating structure with an iris-loaded waveguide, the relationship between the field strength E and power P along the longitudinal position z is required. By further considering the beam loading effect, the corresponding theoretical formula can be expressed as follows:

$$\begin{cases} E(z) = \sqrt{2\alpha Z_{\mathrm{s}} P(z)} \\ \frac{\mathrm{d}P(z)}{\mathrm{d}z} = -2\alpha P(z) - IE(z) \end{cases} \tag{1}$$

where α is the attenuation factor, Z_{s} is the shunt impedance, and I is the average beam current.

The field strength distribution must be designed according to the quality requirements of the output electrons. The longitudinal motion of electrons under field strength is expressed as follows:

$$\begin{cases} \frac{\mathrm{d}\gamma}{\mathrm{d}z} = -\frac{eE}{m_0c^2}\sin\varphi \\ \frac{\mathrm{d}\varphi}{\mathrm{d}z} = \frac{2\pi}{\lambda}\left(\frac{1}{\beta_{\mathrm{p}}} - \frac{\gamma}{\sqrt{\gamma^2-1}}\right) \end{cases} \tag{2}$$

where γ is the relativistic mass factor, φ is the phase, e is the electron charge, m_0c^2 is the rest energy of the electron, λ is the RF wavelength, and β_{p} is the cavity phase velocity.

Beam dynamics mainly involves studying the radial motion of electrons, and the transverse motion equation of electrons in the RF linear accelerator can be expressed as follows:

$$\frac{\mathrm{d}}{\mathrm{d}z}\left(\beta\gamma R'\right) + \frac{e}{m_0c^2}Q(z)R = \frac{\varepsilon_{\mathrm{r}}^2}{\beta\gamma R^3} \tag{3}$$

where β is the electron phase velocity, R is the beam radius, R' is the first derivative of the beam radius, Q is the radial focusing force coefficient, and ε_{r} is the radial beam emittance of the electron beam with a value equal to $\beta\gamma$ times the geometric phase space emittance. For a group of electrons with the same longitudinal initial conditions (initial phase and energy), the ε_{r} that describes its collective properties is constant and remains unchanged in motion. Equation (3) can also be written as follows:

$$\frac{\mathrm{d}^2R}{\mathrm{d}z^2}=-\frac{1}{\beta^2\gamma}\frac{\mathrm{d}\gamma}{\mathrm{d}z}\frac{\mathrm{d}R}{\mathrm{d}z}-\frac{eR}{\beta\gamma m_0c^2}Q(z)+\frac{\varepsilon_{\mathrm{r}}^2}{\beta^2\gamma^2R^3} \tag{4}$$

For convenience, the length of each cavity was divided into 100 equal parts, in which γ and φ were considered constant.

As the most important component, the entire linac is mainly determined by the TW accelerating structure, which must be precisely designed and optimized; a detailed description is provided in the next section.

3 TW accelerating structure optimization based on a genetic algorithm

As mentioned in Sect. 2, the core of an RF linac is a TW accelerating structure, which refers to a cavity chain composed of a series of iris-loaded waveguides. Electrons affected by the iris can accelerate synchronously. The acceleration performance of the electron beam in the TW accelerating structure depends on the phase velocity distribution and cavity structure of the cavity chain, which are necessary for optimization.

3.1 Cavity chain optimization based on a genetic algorithm

As repeated attempts to design a TW accelerating structure based on engineering experience are time-consuming, and it is difficult to obtain the optimal parameters, a highly-effective solution is provided by a MOGA. In the MOGA, a fitness function based on the optimization objectives was formulated. Subsequently, 200 individual populations were initialized at varying velocities. By computing the fitness function, rapid non-dominated sorting, crowding distance calculation, and genetic operations, a set of individual solutions with the smallest non-dominated index was generated over 30 generations. In the genetic operations, a binary tournament selection method was employed for the selection process, and a single-point crossover method was used for the crossover operation with a probability typically ranging from 0.5 to 1.0; in this context, a value of 0.6 was adopted. Additionally, a single-point mutation method was applied for the mutation operation, with a mutation probability generally ranging from 0 to 0.05; in this case, a value of 0.001 was chosen. A low-energy linear accelerator requires a variable phase velocity structure to achieve electron capture. As the linac designed in this context is mainly applied to the on-site NDT of electrical equipment, considering the energy required for X-ray penetration and the influence of radiation in the application process of electrical equipment, the capture rate, energy spread, and output energy were considered the optimization objectives for designing the accelerator cavity chain. Additionally, the proposed universal method can be extended to the design of other linacs by adjusting the optimization objectives. To obtain a high capture ratio, the distribution in the cavity chain must be reasonably designed. The design parameters are listed in Table 1.

Table 1 Overall design parameters

Parameter	Value
Frequency (GHz)	9.3
Operating mode	$2\pi/3$
TW accelerating structure length (cm)	< 50
Number of cavities	< 50
Kinetic energy (MeV)	~3
Current (mA)	~200
Energy spread	~10%
Capture ratio	~90%

Table 2 Power source parameters

Parameter	Value
Peak power (MW)	1
Duty ratio	0.8%
Pulse width (μs)	10

According to Eqs. (1) and (2), discrete recurrence can be performed to calculate the electron beam parameters along the axis of the TW accelerating structure. These formulas, which consider the loading effect of the beam, have a good calculation accuracy. The initial energy generated by the electron gun was 30 keV. A MOGA was employed to determine the optimal phase velocity distribution. To simplify the structural design and engineering implementation, an equivalent structure was adopted. In the design process, the adoption of a constant iris radius, which was set to $0.1\times\lambda$=3.2236 mm, significantly streamlined the workload during the design and manufacturing processes. Simultaneously, under the conditions satisfying the design objectives, six segments of equal cell length were selected corresponding to the phase velocity by comprehensively considering the computational efficiency, engineering costs, and quantities. The power source parameters are listed in Table 2.

The eight pareto front points obtained using the NSGA-II are shown in Fig. 2. The corresponding capture ratios ranged

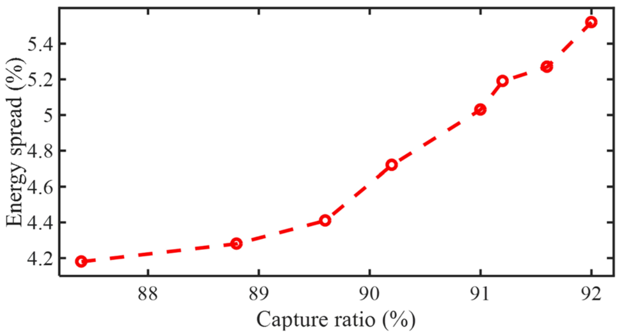

Fig. 2 (Color online) Genetic algorithm results of cavity chain optimization

from 87.4% to 92.0%, and the energy spread ranged from 4.18% to 5.52%.

The fourth point, from right to left, was the focal point for analyzing the trajectory of electrons within the instance of an elliptical diaphragm and a straight edge cavity. The changes in the phase and energy with respect to the longitudinal position of the TW accelerating structure are shown in Fig. 3a and b.

Figure 3a shows that a phase width of 328.3° starting from an initial phase width of 360° was successfully captured with a capture ratio of 91.2%. The phases of the captured electrons oscillated in the first half of the cavity chain. After 0.1 m in the longitudinal direction, the phase gradually decreased and became stable. As shown in Fig. 3b, the energy of the captured electrons oscillated in the initial half. However, beyond 0.1 m along the longitudinal position, the phase gradually stabilized and the energy increased approximately linearly.

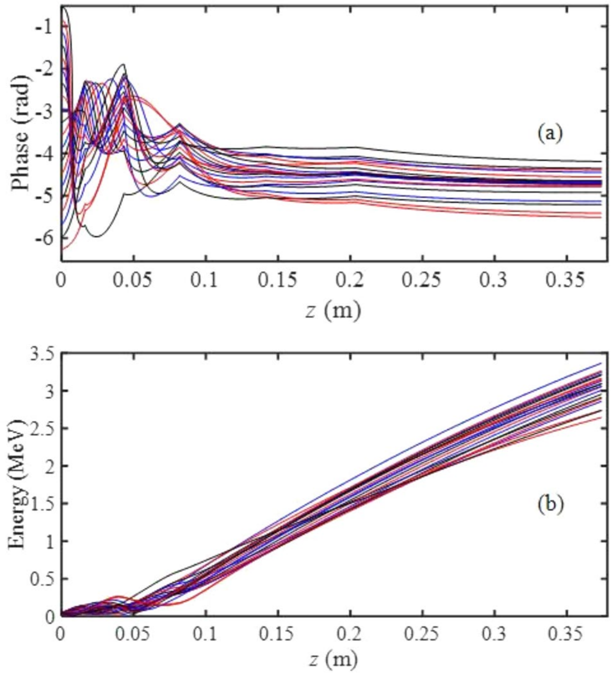

Fig. 3 (Color online) Changes in **a** phase and **b** energy with respect to the longitudinal position *z* of the TW accelerating structure

3.2 Structural optimization based on a genetic algorithm

Determined from the phase velocity and resonant frequency, *D* and *b* were fixed in advance. The other structural parameters, *a*, *t*, *g*, and the cavity shape were optimized in the design. To represent the cavity parameters visually, the dimensions are shown in Fig. 4a. Optimizing the structural parameters fundamentally entails adjusting the microwave parameters of the cavity, such as the shunt impedance and attenuation factor. The variation in the field intensities of each cavity caused by different microwave parameters influences the overall performance of the linac, such as the capture ratio and energy spread.

When the structural parameters of the cavity were changed, a non-dominated solution set was obtained based on the NSGA-II, as shown in Fig. 5.

Figure 5 shows that the non-dominant solution set of the capture ratio and energy spread differed for different iris radii *a*, iris thicknesses *t*, iris chamfer widths *g*, irises, and cavity shapes. When *a*=3.0 mm, the capture ratio and corresponding energy spread were both relatively high. When the required capture ratio was less than 91.2%, a smaller iris thickness could be used to obtain a smaller energy spread. In Fig. 5d, Case I indicates that the iris was elliptical and the cavity had a straight edge; Case II indicates that the iris was circular and the cavity had a straight edge; and Case III indicates that the iris was circular and the cavity was semicircular. When the capture ratio was greater than 90.5%, the beam accelerated by the circular iris and semicircular cavity structure had a small energy spread.

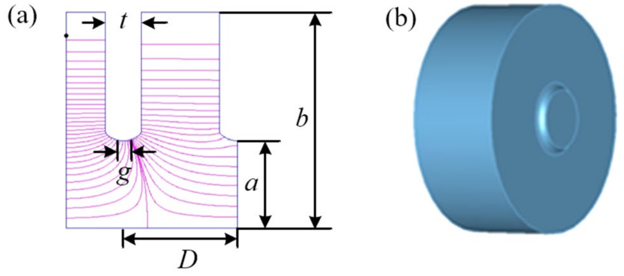

Fig. 4 (Color online) **a** 1.5-cavity two-dimensional model and **b** single-cavity three-dimensional model

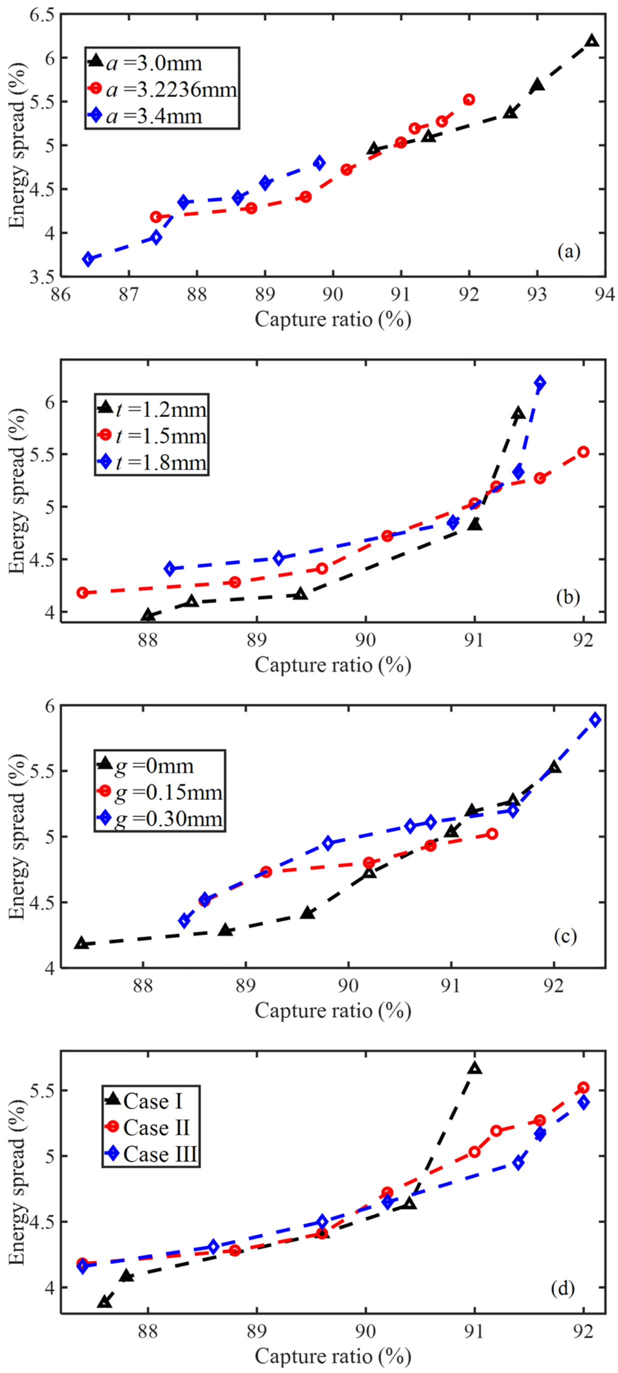

Fig. 5 (Color online) Pareto solution set: **a** change *a*, **b** change *t*, **c** change *g*, and **d** change shape

For convenience, $a = 3.2236$ mm, $t = 1.5$ mm, $g = 0$ mm, and the circular iris and straight edge cavity were adopted. The structural parameter indices are listed in Table 3.

Table 3 Cavity size parameters

Parameter	Value
a (mm)	3.2236
t (mm)	1.5
g (mm)	0
Shape	Circular iris and straight edge cavity

4 Design of other key components

In addition to the TW accelerating structure, the key components of the accelerator include focusing coils, an electron gun, and RF couplers, the layout of which is shown in Fig. 1. A magnetic field is required to focus the beam, and focusing coils are often used to generate the magnetic field. In addition, an electron gun is required to provide the initial beam, and RF couplers are required to feed the microwave power.

4.1 Focusing coils

During acceleration, the transverse size of the electron must be limited to an acceptable range. Therefore, the focusing coil must be designed to generate a magnetic field. Considering the engineering processing and installation intervals, seven coils with spacings of 0.4 cm were designed.

In the physical design of the transverse motion, the numerical calculation of the beam radius curve $R(z)$ using Eq. (4) is critical for the physical design. For this purpose, ε_r must be obtained at the electron gun exit, which is considered invariant in the calculation. As electrons with different initial phases have different φ and γ values, the calculation must be performed separately for various initial phases. The focusing magnetic field overcomes the defocusing effect of $Q(z)$ and constrains the beam radius within a small range.

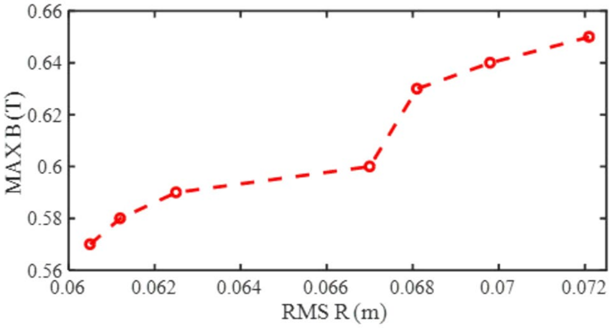

Fig. 6 (Color online) Genetic algorithm results of coil optimization

This facility comprised seven coils with adjustable ampere turns at fixed positions. The independent variable was a Gaussian distribution with seven fixed positions corresponding to the multi-objective algorithm. The superposition of these coils controlled the longitudinal magnetic field. In addition, the root mean square value of the outlet beam envelope and the sum of the external magnetic intensities were set as objective functions that were as small as possible. The results of the algorithm are shown in Fig. 6.

The fourth pareto front, from left to right, was selected, and its magnetic field distribution is shown in Fig. 7. The maximum magnetic field was no more than 0.25 T, and the magnetic field decreased to 0 at $z = -10$ cm.

Under the initial electron conditions, ε_r was 6 mm · mrad; R and R' were 1 mm and 0 mm, respectively; the initial energy was 30 keV with a 200 mA current; and the initial phase had six points of $-360° \sim -32°$. The transverse radius curves are presented in Fig. 8, where the colors and lines are used to differentiate the electrons with distinct initial phases.

Figure 8 shows that the transverse radius curves varied for the electrons with distinct initial phases. The maximum exit radius occurred when the initial phase was −32.0°, whereas the minimum exit radius was observed at an initial phase of −294.4°. The exit radius of the initial phase in one cycle was less than 2 mm, satisfying the requirements.

4.2 Electron gun

As another key component, an electron gun was designed to provide the initial electron beams. The source electron beam affects the acceleration structure at the back end and beam mass at the exit of the linac. Considering that the beam energy of the low-energy accelerator designed in this study was 3 MeV, the peak intensity of the electron gun output beam was set at 200 mA to ensure that the output beam power reached the kilowatt range. The electron gun must simultaneously accelerate the electron beam to 30 keV to satisfy the parameter requirements of the posterior acceleration structure.

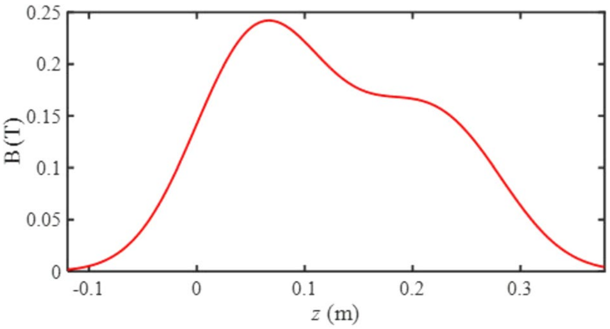

Fig. 7 (Color online) Magnetic field distribution

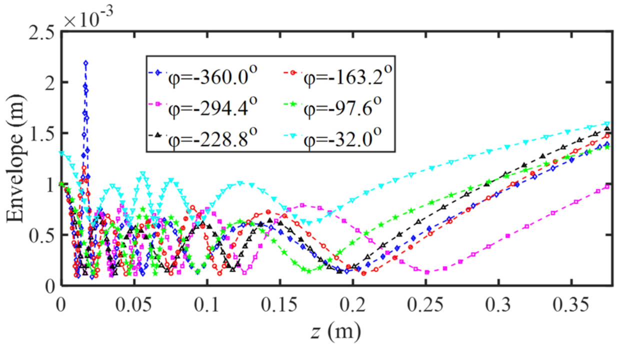

Fig. 8 (Color online) Beam transverse radius curves

In the design process, to prevent high field strength at the tip and mitigate the risk of electron gun vacuum breakdown and equipment damage, an edge chamfering treatment was applied to the focusing pole and anode head in the electric field. The maximum surface electric field was considered in the design of the electron gun. There were two common electron gun structures near the anode hole, with and without nose cones. Nose cones affect the maximum surface electric field. The results of the two simulation models are shown in Fig. 9.

Figure 9 shows that the maximum field strength was 8.61 MV/m when the nose cone was incorporated, compared to 9.72 MV/m when the nose cone was omitted. Consequently, the nose cone structure effectively diminished the maximum surface electric field and enhanced the quality of the induced beam.

Owing to the small structure of the electron gun, vacuum breakdown and other phenomena may occur. To achieve a well-founded electron gun design, a comprehensive analysis of both internal and surface field distributions is necessary. The final electron gun design with a 200 mA beam current is shown in Fig. 10.

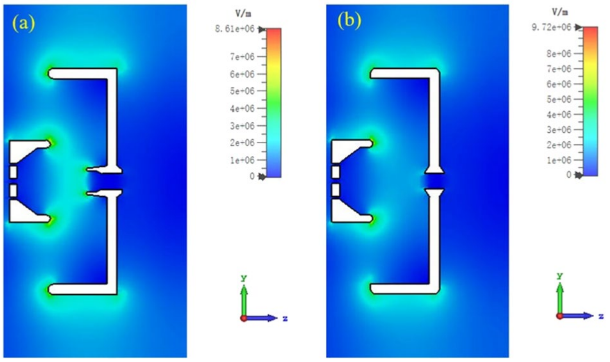

Fig. 9 (Color online) Electric field distribution cloud map: **a** with a nose cone and **b** without a nose cone

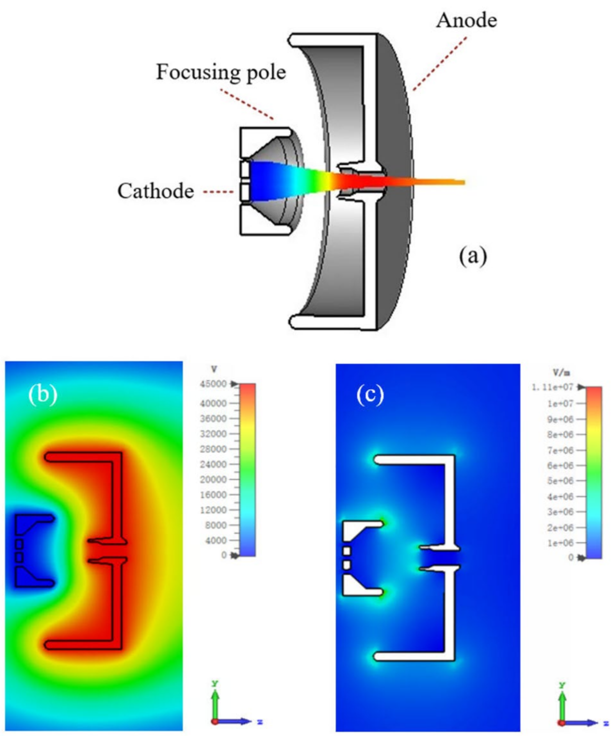

Fig. 10 (Color online) Electron gun design: **a** beam trajectory, **b** electric potential, and **c** electric field

Figure 10a shows that the beam focusing performance was commendable and the designed electron gun could reach a beam radius of 1 mm after traveling 20 mm in the longitudinal direction from the anode. Figure 10c shows that the electric fields at the cathode head, anode head, and nose cone had large values.

4.3 RF couplers

CST Microwave Studio software was used to design the input and output couplers. The input coupler was linked to the cavity at a phase velocity of 0.38, while the output coupler was connected to the cavity at a phase velocity of 0.99. For analytical convenience, a symmetrical model of the output coupler comprising four cavities was established, as shown in Fig. 11.

Standing wave fields were present in the two cavities on both sides, and traveling wave fields were present in the two cavities in the middle. Thus, the four-cavity symmetrical model in the working mode $2\pi/3$ formed one period. In the CST simulation for the entire accelerator, the coupling factor became 1.0202, which is slightly different from the original designed value of 1.0362 obtained using the four-cavity model. Figure 12 shows the S-parameters obtained using the frequency-domain solver. The reflection coefficient was approximately −56 dB, and the transmission coefficient was approximately 0 dB at a frequency of 9.3 GHz. Most of the microwave energy was fed into the TW accelerating structure.

In this context, a unilateral eccentric structure was used to alleviate field asymmetry. Figure 13 presents the distributions of the normalized field intensity and phase at the center of the coupling cavity along the reference circle for eccentricities of 0, 0.42, and 0.5 mm, respectively. As shown in Fig. 13a, the field asymmetry was weakened by setting a certain eccentricity. In the three cases with different eccentricities, the field asymmetry was ($e = 0.42$ mm) < ($e = 0.5$ mm) < ($e = 0$ mm), in descending order. Figure 13b shows that eccentricity had a minimal impact on the phase of the field strength. Considering that the motion of electrons in the TW structure is mainly affected by the asymmetry of the field amplitude, it is feasible to adopt a unilateral eccentric structure with an eccentricity of 0.42 mm for reducing the impact of field asymmetry on electron motion.

Considering the impact of field asymmetry, it is essential to conduct a simulation analysis of the entire model with the completion of the design of the output and input couplers.

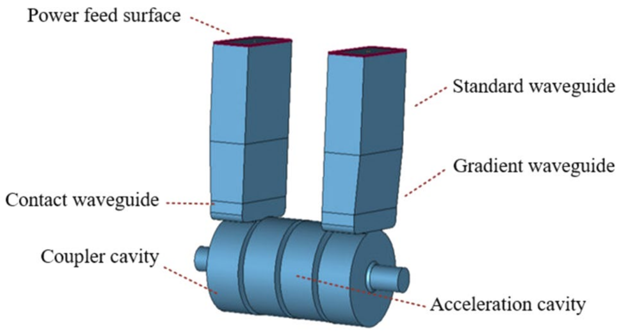

Fig. 11 (Color online) Four-cavity symmetrical model of the output coupler

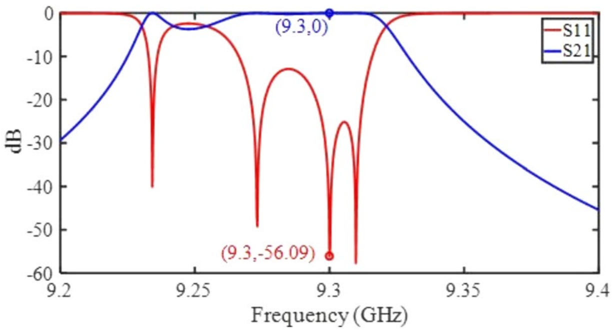

Fig. 12 (Color online) S-parameters obtained by the frequency-domain solver

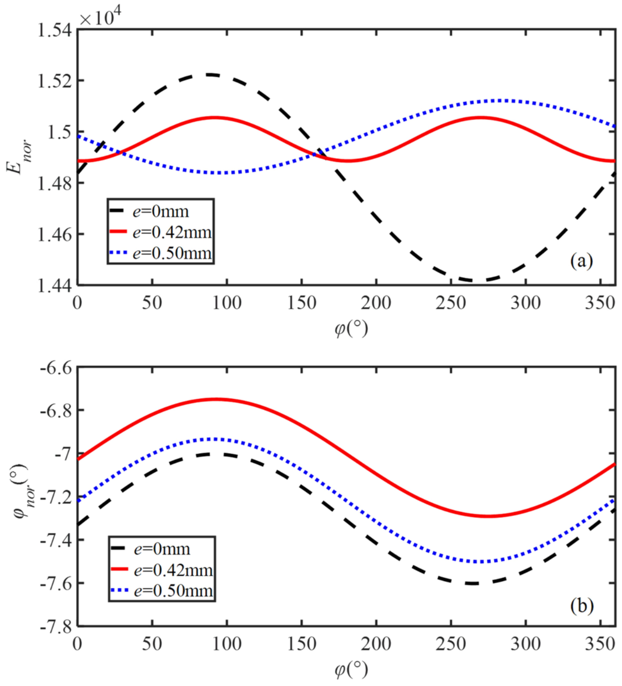

Fig. 13 (Color online) Coupling cavity structures under different eccentricities: **a** field intensity amplitude distribution and **b** field intensity phase distribution

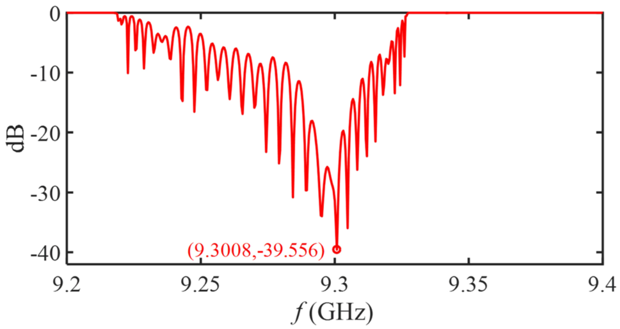

Fig. 14 (Color online) S-parameter distribution for the entire accelerating structure

Figure 14 presents the S-parameter distribution for the entire accelerating structure.

As shown in Fig. 14, the overall three-dimensional electromagnetic field model, including the TW accelerating structure and coupler, had a minimum peak when the frequency was 9.3008 GHz, which satisfied the operating mode. Furthermore, multiple peaks in the S-parameter corresponded to different operational modes. To facilitate a comprehensive analysis of the entire TW accelerating structure, Fig. 15 illustrates the distribution of the field strength and phase.

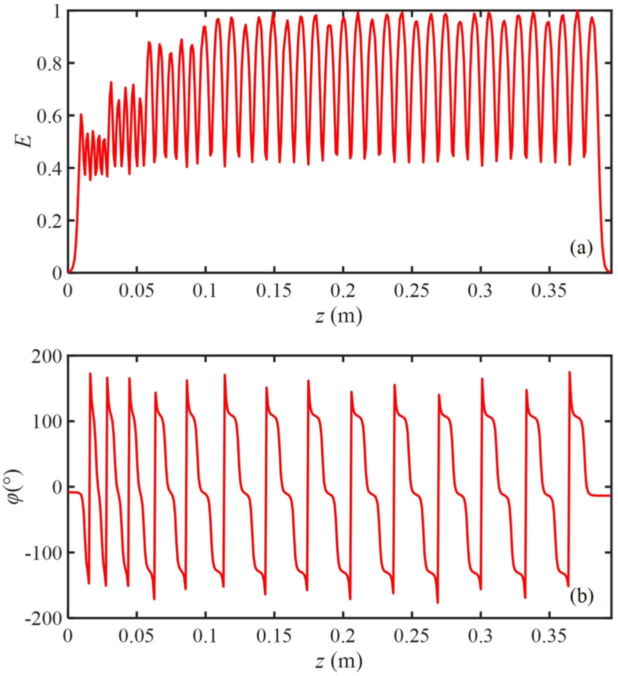

Fig. 15 (Color online) Integral pipe parameters: **a** field strength and **b** phase

Figure 15a illustrates the longitudinal distribution of the amplitude of the central field intensity, which was relatively modest in the first half of the longitudinal distance, but gradually increased and stabilized in the second half. As the individual coupling cavity was approximately 60° and the single acceleration cavity was close to 120°, the combined phase of the two coupling cavities and the 41 acceleration cavities spanned 14 cycles, as shown in Fig. 15b.

5 Beam dynamics simulations

In the computation of the TW accelerating structure described in Sect. 3, the space-charge effect was not considered, and the calculation model was one-dimensional. To obtain more precise results, it is imperative to employ the specialized beam dynamics simulation software PARMELA for multi-electron calculations that consider the space-charge effect. The electrons introduced into the TW accelerating structure were derived directly from the electron gun results. At the entrance of the electron gun, the macro-electron number was set to 10274 with a beam current of 200 mA. The results are shown in Fig. 16.

Figure 16 shows that the exit phase width was relatively bunched with an exit energy of 2.92 MeV. As listed in Table 4, the capture ratio and energy spread were 95.00% and 7.15%, respectively.

Fig. 16 (Color online) PARMELA simulation results for the 200 mA beam current

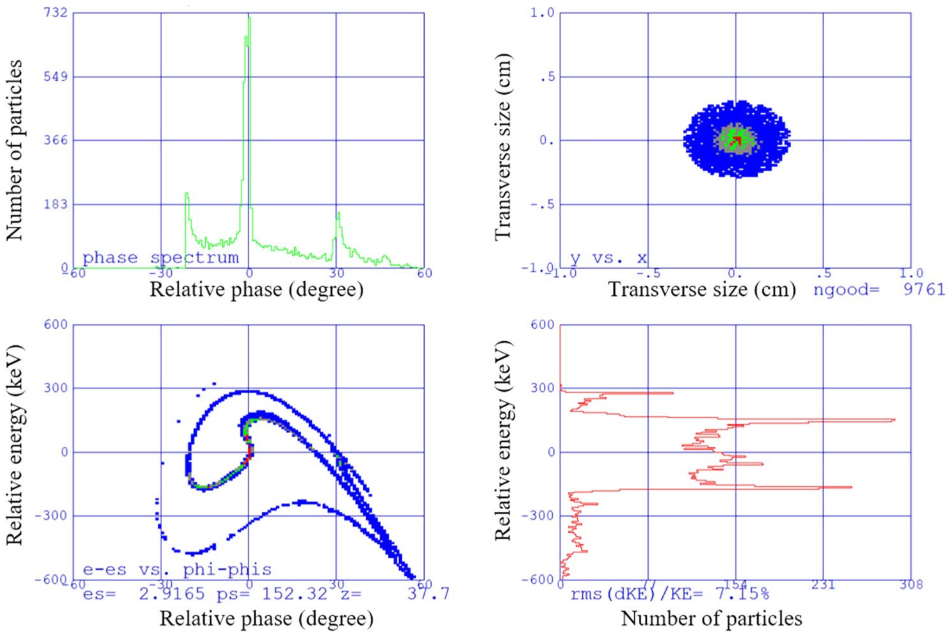

Table 4 Results of different simulation models

/	Capture ratio (%)	Energy spread (%)	Average energy (MeV)
Single-particle model	91.20	5.19	3.07
Multi-particle model	95.00	7.15	2.92

Table 5 Optimization results under different phase velocity distributions

Phase velocity distribution	Capture ratio (%)	Energy spread (%)	Average energy (MeV)
1st	95.00	7.15	2.92
2nd	94.82	21.42	2.89
3rd	93.98	8.83	2.89

Table 4 shows that the average energy values under the multi-particle model were consistent with those under the single-particle model, whereas the energy spread and capture ratio were slightly larger. Owing to the correlation between the longitudinal and transverse motions, electrons focused in the transverse direction could be extracted in the longitudinal direction. Additionally, the electron gun beam was focused when injected into the TW accelerating structure with negative-angle beam injection, and the focus was in the coupling cavity, which contributed to a high capture ratio. Thus, the capture ratio obtained from the multi-particle simulations surpassed the simulation results of the single-particle model. In addition, multi-particle simulations considering the space-charge effect resulted in a higher energy spread.

To validate the outcomes of the algorithm, adjustments were made to the phase velocities for specific segments, such as replacing 0.38 with 0.42 for the second segment and 0.50 with 0.52 for the third segment. The optimization results for the capture ratio, energy spread, and average energy under different distributions are listed in Table 5.

The first phase velocity distribution had the optimal beam parameters, which indicates that the optimization outcome based on the MOGA is reliable.

6 Conclusion

A versatile MOGA under multiple constraints was introduced for the design of TW accelerator cavity chains, which can be expanded as a universal technology for linacs with bunching sections. In view of its application to the on-site NDT of electrical equipment, an X-band linac with a low-energy spread and high capture rate was successfully designed. Therefore, the accelerator cavity chain was segmented to simplify both design and fabrication. To constrain the transverse beam spread in TW accelerator structures, focusing coils optimized for the beam spot size were devised to achieve beam focus. In addition, a single-sided eccentric coupler was engineered to establish electric fields within TW accelerator structures. Furthermore, an electron gun was designed to supply electrons to the accelerator cavity chain. Another low-energy spread X-band linac was designed, as described in Appendix A, using the same MOGA under multiple constraints, which further demonstrates the universality of the proposed design methodology.

Consequently, a versatile MOGA under multiple constraints was proposed for the design of TW linacs with optimization objectives tailored to specific operational requirements. Notably, the proposed design method not only guides the specific accelerator design discussed in this context but can also be utilized as a general approach for related designs according to various design demands.

Appendices

Appendix A: MOGA generality

As mentioned previously, the primary contribution of this study is the development of a MOGA under multiple constraints for the design of linac cavity chains. The design methodology and approach can be extended as a general technology to simplify the design of linacs with bunching sections, and specific optimization objectives can be chosen and determined based on different application scenarios and requirements. The X-band linac designed for NDT of electrical devices in the main text serves as an illustrative example of the proposed method. Application goals and constraints can be tailored according to specific application requirements. To verify the generality the MOGA method proposed in this context, a low-energy-spread X-band linac was designed for other applications; therefore, the output energy and energy spread were taken as the optimization objectives.

In this design example, both the number of segments and cavities per segment were set as independent variables. The other algorithm parameters are the same as those in the main text. The designed accelerator cavity structure is shown in Fig. 4. The final optimized results were obtained after 50 iterations. The five pareto front points obtained using the NSGA-II are shown in Fig. 17. The corresponding energy spread ranged from 1.13% to 3.12%, and the energy ranged from 2.64 to 2.96 MeV.

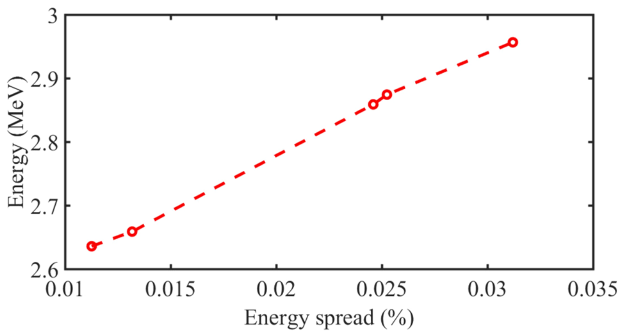

Fig. 17 (Color online) Five pareto front points obtained by NSGA-II

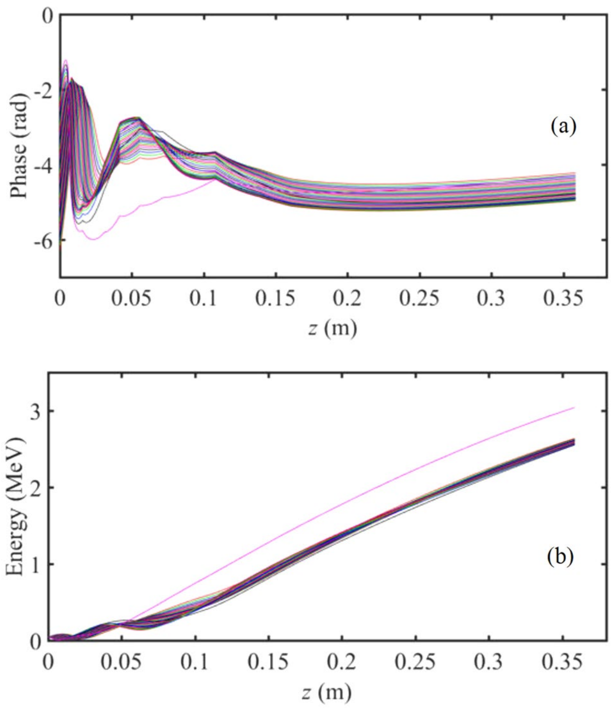

Fig. 18 (Color online) Coupling cavity structures under different eccentricities: **a** field intensity amplitude distribution and **b** field intensity phase distribution

The first point in Fig. 17 was selected to design the X-band linac. To analyze the movement of electrons in the TW accelerating structure, the changes in the phase and energy with the longitudinal position are plotted in Fig. 18.

Figure 18a shows the capture of a phase width of 200.1° from an initial 360° phase width, achieving a capture ratio of 69.4%. The captured electrons exhibited phase oscillations in the first half of the cavity chain and stabilized longitudinally after traversing 0.1 m from the entrance. Figure 18b shows that the energies of the captured electrons oscillated in the first half. As the phase gradually stabilized after 0.1 m in the longitudinal position, the energy increased approximately linearly. The final design consisted of an exit energy of 2.61 MeV and an energy spread of 1.24%.

Thus, the work described in Appendix A further validates that the universal approach proposed in the main text can be extended to different design demands for various applications and only needs to modify the optimization objectives and design conditions.

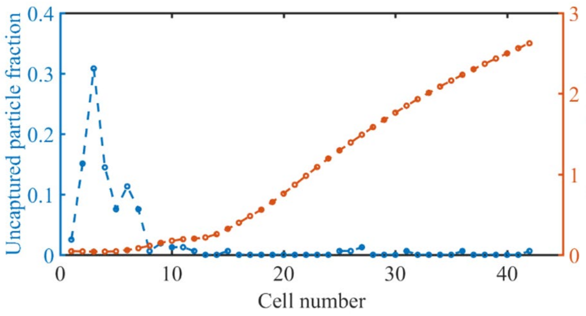

Fig. 19 (Color online) Uncaptured electron fraction and electron acceleration energy with cavity number

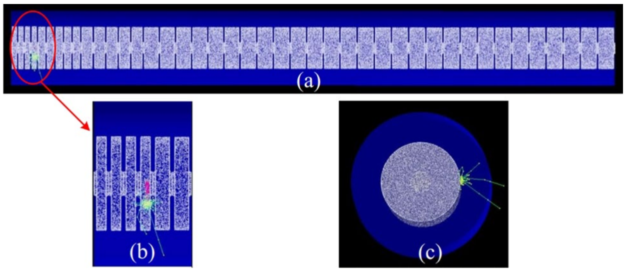

Fig. 20 (Color online) Radiation calculation process: **a** longitudinal plane diagram, **b** zoomed in on the details of the 1~6 cell, and **c** cross-sectional drawings

Appendix B: Radiation effects of the uncaptured electrons in the linac

On-site NDT is typically conducted under controlled environmental conditions and involves precise control of X-ray radiation generation, transmission paths, and beam energy. This ensures minimal impact of radiation on the electronic components surrounding the object being tested during inspection. Enhancing electron capture rates is one of the measures aimed at reducing the radiation effects on components and human beings near the tested object. To validate the influence of the uncaptured beam, GEANT4 was used to analyze the radiation effects caused by uncaptured electrons.

For the low-energy spread design scheme proposed in Appendix A, the energy and proportion of electrons lost in different cells of the linac have were calculated, and the statistical results are shown in Fig. 19. Figure 19 shows that the particle losses were concentrated before the eighth cell, with the highest losses occurring in the fourth cell, where the central energy was approximately 100 keV. To simplify the analysis, the beam energy and transverse radius were set to 100 keV and 1 mm in GEANT4, respectively. To analyze the radiation effects caused by the uncaptured electrons, it was assumed that the lost electrons impacted the inner wall of the cell rather than the disk; thus, the electrons were emitted radially in GEANT4. To simplify the calculation process, it was assumed that all uncaptured electrons were lost in the fourth cell, and the calculated results are shown in Fig. 20. Using a source of 10^8 electrons, the calculated maximum dose deposition on the outer wall of the linac was 9.75×10^{-7} Gy/h.

Taking the X-band linac design proposed in Appendix A as an example, the linac yielded an output energy of 2.61 MeV, energy spread of 1.24%, and capture rate of 69.4%. The beam current was 200 mA, the macro-pulse width was 10 μs, and the repetition rate was 100 Hz. The resulting maximum dose deposition on the outer wall of the accelerator tube was calculated to be 37.2 Gy/h. During the on-site NDT of electrical equipment, the scanning time is sustained from a few minutes to 30 min [32]. Taking 30 min as an example, the cumulative dose deposited from the lost electrons was 18.66 Gy. NDT processes often require multiple scans, resulting in a cumulative dose far exceeding 18.66 Gy. Typically, surrounding electronic equipment is affected when the deposition dose exceeds 20 Gy [33, 34]. In addition, according to the International Atomic Energy Agency (IAEA) Radiation Protection and Safety of Radiation Sources: International Basic Safety Standards, the human body should not absorb more than 2 Gy within two days [35]. Furthermore, additional lead shielding around the linac can reduce radiation exposure, increase the volume and weight of the accelerator, and consequently increase costs, which is not conducive to on-site NDT. Thus, it is essential to consider a high capture ratio as an optimization objective.

Author Contributions All authors contributed to the study conception and design. Material preparation, data collection, and analysis were performed by Haimeng Wang, Yifeng Zeng, Hao Hu, Junyang Li, and Tongning Hu. The first draft of the manuscript was written by Haimeng Wang, Yifeng Zeng, Hao Hu, and Tongning Hu, and all authors commented on previous versions of the manuscript. All authors read and approved the final manuscript.

Data Availability The data that support the findings of this study are openly available in Science Data Bank at https://cstr.cn/31253.11.sciencedb.34126 and https://doi.org/10.57760/sciencedb.34126.

Declarations

Conflict of interest The authors declare that they have no conflict of interest.

References

1. A.S.N. Huda, S. Taib, K.H. Ghazali et al., A new thermographic NDT for condition monitoring of electrical components using ANN with confidence level analysis. ISA T. **53**(3), 717–724 (2014). https://doi.org/10.1016/j.isatra.2014.02.003
2. Y. Chou, L. Yao, Automatic diagnostic system of electrical equipment using infrared thermography. In *2009 International*

Conference of Soft Computing and Pattern Recognition, Malacca, Malaysia, 4–7 December 2009. https://doi.org/10.1109/SoCPaR.2009.41

3. Y. Cao , X.M. Gu , Q. Jin, Infrared technology in the fault diagnosis of substation equipment. In *2008 China International Conference on Electricity Distribution*, Guangzhou, China, 10–13 December 2008. https://doi.org/10.1109/CICED.2008.5211792
4. B.S. Li, X.H. Zhu, S.T. Zhao et al., HV power equipment diagnosis based on infrared imaging analyzing. In *2006 International Conference on Power System Technology*, Chongqing, China, 22–26 October 2006. https://doi.org/10.1109/ICPST.2006.321512
5. E.G. Costa, T.V. Ferreira, M.G.G. Neri et al., Characterization of polymeric insulators using thermal and UV imaging under laboratory conditions. IEEE Trans. Dielectr. Electr. Insul. **16**(4), 985–992 (2009). https://doi.org/10.1109/TDEI.2009.521184
6. Z.Y. Li, L.C. Li, X.L. Jiang et al., Effects of different factors on electrical equipment UV corona discharge detection. Energies **9**(5), 369 (2016). https://doi.org/10.3390/en9050369
7. F.Y. Tian, Y.P. Hao, Z.Y. Zou et al., An ultrasonic pulse-echo method to detect internal defects in epoxy composite insulation. Energies **12**(24), 4804 (2019). https://doi.org/10.3390/en12244804
8. T. Bouchala, B. Abdelhadi, A. Benoudjit, Novel coupled electric field method for defect characterization in eddy current non-destructive testing systems. J. Nondestruct. Eval. **33**(1), 1–11 (2014). https://doi.org/10.1007/s10921-013-0197-5
9. H. Yu, J. Wei, X.P. Zhao et al., The perspective detection of the X-ray digital radiography for the electrical equipment. In *2012 International Conference on High Voltage Engineering and Application*, Shanghai, China, 17–20 September 2006. https://doi.org/10.1109/ICHVE.2012.6357096
10. X.H. Pang, Y.X. Qi, X.F. Li et al., Research on defect pattern recognition of GIS equipment based on X-ray digital imaging technology. In *2018 International Conference on High Voltage Engineering and Application*, Athens, Greece, 10–13 September 2018. https://doi.org/10.1109/ICHVE.2018.8641973
11. Y. Mitsuya, M. Uesaka, K. Dobashi et al., Non-destructive testing of bridges with compact X-band electron Linac-based X-ray sources. J Kensa Gijutsu. **24**(1), 65–70 (2019)
12. T.N. Hu, H.M. Wang, Y.F. Zeng et al., Fault locating for traveling wave accelerators based on transmission line theory. Nucl. Sci. Tech. **34**, 116 (2023). https://doi.org/10.1007/s41365-023-01279-z
13. T.N. Hu, Y.J. Pei, G.Y. Feng, Electron beamline of a Linac-based injector applied to a compact free electron laser-terahertz radiation source. Jpn. J. Appl. Phys. **57**(10), 100310 (2018). https://doi.org/10.7567/JJAP.57.100310
14. X. Li, J.Q. Zhang, G.Q. Lin et al., Performance of an electron linear accelerator for the first photoneutron source in China. Nucl. Sci. Tech. **30**, 4 (2019). https://doi.org/10.1007/s41365-019-0576-4
15. J.H. Yang, Y. Yang, C.Q. Wang et al., Research and development of X-band 6 MeV RF linear accelerating tube. Atomic Energy Sci. Technol. **55**, S2 (2021) (in Chinese)
16. X. Huang, W.C. Fang, Q. Gu et al., Design of an X-band accelerating structure using a newly developed structural optimization procedure. Nucl. Instrum. Methods. Phys. Res. A. **854**, 45–52 (2017). https://doi.org/10.1016/j.nima.2017.02.050
17. S.V. Kutsaev, Novel technologies for compact electron linear accelerators (review). Instrum. Exp. Tech. **64**(5), 641–656 (2021). https://doi.org/10.1134/S0020441221050079
18. S.V. Kutsaev, R. Agustsson, A. Arodzero et al., Compact X-Band electron Linac for radiotherapy and security applications. Radiat. Phys. Chem. **185**, 109494 (2021). https://doi.org/10.1016/j.radphyschem.2021.109494
19. X.C. Lin, H. Zha, J.R. Shi et al., A compact X-band backward traveling-wave accelerating structure. Nucl. Sci. Tech. **35**, 5 (2024). https://doi.org/10.1007/s41365-024-01403-7
20. G. Gatti, A. Marcelli, B. Spataro et al., X-band accelerator structures: on going R&D at the INFN. Nucl. Instrum. Methods. Phys. Res. A. **829**, 206–212 (2016). https://doi.org/10.1016/j.nima.2016.02.061
21. X.W. Wu, J.R. Shi, H.B. Chen, High-gradient breakdown studies of an X-band Compact Linear Collider prototype structure. Phys. Rev. ST Accel. Beams. **20**(5), 052001 (2017). https://doi.org/10.1103/PhysRevAccelBeams.20.052001
22. M. Volpi, N. Catalan-Lasheras, A. Grudiev et al., High power and high repetition ratio X-band power source using multiple Klystrons. In *9th International Particle Accelerator Conference*, Vancouver, Canada, 3 May 2018. https://doi.org/10.18429/JACoW-IPAC2018-THPMK104
23. S. Kim, Y. Lee, G. Kim et al., Development of a compact X-band linear accelerator system mounted on an O-arm rotating gantry for radiation therapy. Rev. Sci. Instrum. **92**(2), 024103 (2021). https://doi.org/10.1063/5.0030271
24. X.C. Lin, H. Zha, J.R. Shi et al., Fabrication, tuning, and high-gradient testing of an X-band traveling-wave accelerating structure for VIGAS. Nucl. Sci. Tech. **33**, 102 (2022). https://doi.org/10.1007/s41365-022-01086-y
25. T.N. Hu, Y.J. Pei, G.Y. Feng, Bunch length evaluation for typical low-energy beam injectors based on RF-phasing techniques. Nucl. Instrum. Methods. Phys. Res. A. **916**, 87–93 (2019). https://doi.org/10.1016/j.nima.2018.10.200
26. K. Deb, A. Pratap, S. Agarwal et al., A fast and elitist multiobjective genetic algorithm: NSGA-II. IEEE Trans. Evol. **6**(2), 182–197 (2002). https://doi.org/10.1109/4235.996017
27. J.H. Wu, N. Hu, H. Setiawan et al., Multi-dimensional optimization of a terawatt seeded tapered free electron laser with a multi-objective genetic algorithm. Nucl. Instrum. Methods. Phys. Res. A. **846**, 56–63 (2017). https://doi.org/10.1016/j.nima.2016.11.035
28. R. Bartolini, M. Apollonio, I.P.S. Martin, Multiobjective genetic algorithm optimization of the beam dynamics in Linac drivers for free electron lasers. Phys. Rev. ST Accel. Beams. **15**(3), 030701 (2012). https://doi.org/10.1103/PhysRevSTAB.15.030701
29. L. Yang, D. Robin, F. Sannibale et al., Global optimization of an accelerator lattice using multiobjective genetical algorithms. Nucl. Instrum. Methods. Phys. Res. A. **609**(1), 50–57 (2009). https://doi.org/10.1016/j.nima.2009.08.027
30. X. Huang, J. Safranek, Nonlinear dynamics optimization with particle swarm and genetic algorithms for spear3 emittance upgrade. Nucl. Instrum. Methods. Phys. Res. A. **757**, 48–53 (2014). https://doi.org/10.1016/j.nima.2014.04.078
31. Z.Y. Dai, Y.C. Nie, Z. Hui et al., Design of S-band photoinjector with high bunch charge and low emittance based on multi-objective genetic algorithm. Nucl. Sci. Tech. **34**, 41 (2023). https://doi.org/10.1007/s41365-023-01183-6
32. X.J. Zhou, R.F. Zhou, P. Li, Industrial CT radiation safety of electron linear accelerator in China Formulation of technical specifications. Standard Science. **02**, 51–53 (2013). https://kns.cnki.net/kcms2/article/abstract?v=2arE9-pF_S0PmHMXOM0GtGCjcs97g4cVYTU_Jb8ilqqtoOReVj8X5QTDhLlp4Ki1KmzwtOfmY7TIYDK2EKw9nTV_nncAOS-BYOdoF8SdccY79OD1DvVEM0tBk5o5kF7ZhnafD5YRI4Usuc-mXKVI5d93BxD3Ehax_PkosJ14DzevADvhuSa7c4TiI-tLArH4&uniplatform=NZKPT&language=CHS(in Chinese)
33. P.E. Dodd, M.R. Shaneyfelt, J.R. Schwank et al., Current and future challenges in radiation effects on CMOS electronics. IEEE Trans Nucl Sci. **57**, 4 (2010). https://doi.org/10.1109/TNS.2010.2042613

34. F. Faccio, Radiation effects in the electronics for CMS. Tutorial Script. (1999)
35. General Safety Requirements. IAEA Safety Standards Series No. GSR Part 3. (2015). https://nucleus.iaea.org/sites/committees/Before%202023%20Archive/TRANSSC/TRANSSC-35-December-11-15_2017/INF-06aAgendaItem251DS496_SPESSStep8_clear.pdf(standards)